Supporting Information

Elucidation of the Structural and Optical Properties of Metal Cation (Na^+, K^+, and Bi^{3+}) Incorporated $Cs_2AgInCl_6$ Double Perovskite Nanocrystals†‡

Parth Vashishtha*[†⊥], Benjamin E. Griffith[‖†⁋⊥], Yanan Fang[†], Ankit Jaiswal[†], Gautam V. Nutan[†], Albert P. Bartók[‖§], Tim White[†] and John V. Hanna*[‖†]

[⊥]P.V. and B.E.G. contributed equally to this work

[†] School of Materials Science and Engineering, Nanyang Technological University, 50 Nanyang Avenue, Singapore 639798, Republic of Singapore

[⁋] Quantum Science Ltd, Techspace One, Daresbury, Warrington, WA4 4AB, United Kingdom

[‖] Department of Physics, University of Warwick, Coventry CV4 7AL, United Kingdom

[§] Warwick Centre for Predictive Modelling, School of Engineering, University of Warwick, Coventry CV4 7AL, United Kingdom

Corresponding Authors: PVashishtha@ntu.edu.sg
J.V.Hanna@warwick.ac.uk

† The experimental data for this study are provided as a supporting dataset from WRAP, the Warwick Research Archive Portal at http://wrap.warwick.ac.uk/160748/.

‡ Electronic supplementary information (ESI) available: Supporting experimental and materials characterization including fully detailed synthesis and instrumental/measurement descriptions, TEM images with particle size and EDXS elemental analyses, measured ^{133}Cs and ^{39}K MAS NMR spectra with tabulated shift, intensity and T_1 data, diagrammatic representation of the T_1 regimes encountered for each system, powder XRD data, and calibration curves relating the ^{133}Cs and ^{39}K experimentally measured shifts and the DFT calculated shieldings. See DOI:10.1039/XXXXXXXX.

Materials

Cesium carbonate (ReagentPlus, 99%), oleic acid (90%), silver acetate (99.99% trace metals basis), indium(III) acetate (99.99% trace metals basis), bismuth(III) acetate (≥99.99% trace metals basis), sodium acetate (99.0% Aldrich), potassium acetate (99.0%, Aldrich), diphenyl ether (ReagentPlus, 99%), benzoyl chloride (ReagentPlus, ≥99%), oleylamine (technical grade,70%),and hexane (anhydrous, 95%) were purchased from Sigma-Aldrich.

Synthesis of Cesium Oleate. A 0.5 M cesium oleate solution was synthesised by mixing cesium carbonate (4075 mg) with OAc (50 mL) loaded in a 3-neck round-bottom flask under inert atmosphere. The reaction mixture was degassed under vacuum at 100 °C for about half an hour followed by heating in nitrogen atmosphere at 150 °C for 3 hours, until the solution becomes clear. The prepared solution was cooled to room temperature, then stored in a vial and kept inside a nitrogen-filled glovebox.

Synthesis of $Cs_2AgIn_xBi_{1-x}Cl_6$ Nanocrystals. For the synthesis of $Cs_2AgInCl_6$ samples, Ag(ac) (0.96 mmol), $In(ac)_3$ (1 mmol), 16 mL of diphenyl ether, 4 mL of the Cs-oleate solution, and 2 mL of Olam were loaded in a three-neck flask and degassed under vacuum for 60 min at 80 °C. Simultaneously, 2 mL of diphenyl ether was dried under vacuum at 50 °C. Subsequently, the system was flushed under N_2, the temperature was slowly increased to 115 °C, and, at this temperature, 800 μL of Bz Cl (6.89 mmol), mixed with 2 mL of degassed DPE, was swiftly injected into the flask. The reaction was quenched after 5 s by cooling with an ice-water bath. Bi-doped $Cs_2AgInCl_6$ samples were prepared using the same protocol but loading the starting reaction mixture with 1 mmol of $In(ac)_3$ and $Bi(ac)_3$ salts in complementary amounts according to the desired percentages. Six different Bi-doped samples were prepared by using the Bi precursor in 0.5, 10, 25, 50, 75 and 90%.

Synthesis of $Cs_2Na_xAg_{1-x}InCl_6$:Bi and $Cs_2K_xAg_{1-x}InCl_6$:Bi Nanocrystals. The total amount of Na(ac)/K(ac) and Ag(ac) must be 0.96 mmol. Na(ac) or K(ac) (x mmol; x= 0, 0.2, 0.4, 0.6, 0.8, and 1), Ag(ac) (1-x mmol), $In(ac)_3$ (1 mmol), $Bi(ac)_3$ (0.05 mmol) 16 ml of diphenyl ether (DPE), 4 ml of the Cs oleate solution, and 2 ml of Olam were loaded in a three-neck reaction flask and degassed under vacuum for 60 min at 80 °C. Simultaneously, an additional 2 ml of DPE was dried under vacuum at 50° C. The system was subsequently flushed under N_2 gas and the temperature was slowly increased to 115 °C. At this temperature a mixture of 800 µl of Bz Cl (6.89 mmol) and the 2 ml of the degassed DPE was swiftly injected into the flask. The reaction was quenched after 5 s by cooling with an ice-water bath.

Purification of the Nanocrystals. All nanocrystals were purified using the same method where the growth solution was first centrifuged at 10,000 rpm for 10 min. The supernatant was discarded and required amounts of the solids were dispersed in 4 mL of anhydrous hexane for optical measurements, whereas the remaining solids were stored under inert atmosphere for additional characterisation.

Materials Characterisation

Transmission Electron Microscopy. A JEOL 2100F was utilized for the HR-TEM and energy dispersive X-ray spectroscopy (EDXS) measurements at an accelerating voltage of 200 kV and beam current of 146 µA. Samples were prepared by dispersing nanocrystals in hexane solvent followed by sonication for 1 min and collection on Cu-200 mesh on forvar grid.

Powder X-ray Diffraction. All powder XRD measurement were performed using a PANalytical X-ray diffractometer equipped with a 1.8kW Cu Kα X-ray tube and operating at 45 kV and 30 mA. The diffraction patterns were measured in air at room temperature using Bragg-Brentano geometry. Each XRD sample was prepared by drop-casting a concentrated solution on a zero diffraction silicon holder.

UV-Vis and PL Measurements. Samples for optical measurements were prepared by diluting the purified solution in 2.5 mL hexane in 1 cm path length quartz cuvettes. A Cary 5000 UV-vis-NIR spectrophotometer and a Cary Eclipse spectrophotometer (slit width = 1 nm, λex = 365 nm) were used. PLQY measurements were conducted using an Ocean Optics QEPro spectrometer and a HAMAMATSU Quantaurus-QY Plus UV–NIR absolute PL quantum yield spectrometer. The optical band gap is estimated by Tauc plots which extrapolate the linear change in the absorption coefficient directly from each UV-vis spectrum.

Solid State NMR. All ^{133}Cs MAS NMR data were acquired at 14.1 and 9.4 T using Bruker Avance II-600 (Larmor frequency ν_o = 78.72 MHz) and Bruker Avance III-400 (Larmor frequency ν_o = 52.47 MHz) spectrometers, respectively, and Bruker 4 mm HX probes operating at a MAS frequency of 12 kHz. At each field the pulse time calibration was undertaken using solid CsCl where a non-selective ('solution') π/2 pulse time of 12 μs was measured corresponding to a selective ('solids') π/2 pulse time 3 μs for the I = 7/2 nucleus. All single pulse ^{133}Cs MAS NMR data were measured using a selective π/6 pulse of 1 μs and a recycle delay of 300 s. Each spectrum was simulated using the DMFit programme.[1] The solid CsCl sample was also used as a secondary chemical shift reference (δ_{iso} 223.2 ppm) against the 0.1 M $CsNO_3$ solution IUPAC primary reference (δ 0.0 ppm).[2] The corresponding ^{133}Cs T_1 measurements were performed using the saturation-recovery pulse technique which utilised a saturation pulse train of 300 π/2 pulses of 3 μs duration, a 1 μs delay between pulses, and a variable τ delay spanning a 0.01 - 1600 s range.

The ^{23}Na MAS NMR data from the $Cs_2Na_xAg_{1-x}InCl_6$:Bi (x = 0.2 - 1) nanocrystal series were acquired at 14.1 and 9.4 T using Bruker Avance II-600 (Larmor frequency ν_o = 158.76 MHz) and Bruker Avance III-400 (Larmor frequency ν_o = 105.81 MHz) spectrometers, respectively, and Bruker 4 mm HX probes operating at a MAS frequency of 12 kHz. The pulse time calibration at each field was undertaken using solid NaCl where a non-selective ('solution')

π/2 pulse time of 4 μs was measured corresponding to a selective ('solids') π/2 pulse time of 2 μs for the I = 3/2 nucleus. All single pulse ^{23}Na MAS NMR data were measured using a selective π/4 pulse of 1 μs and a recycle delay of 30 s. The solid NaCl sample was also used as a secondary chemical shift reference (δ_{iso} 7.0 ppm) against the 0.1 M NaCl solution IUPAC primary reference (δ 0.0 ppm).[2] Accompanying ^{23}Na T_1 measurements were performed using the saturation-recovery pulse technique which utilised a saturation pulse train of 300 π/2 pulses of 2 μs duration, a 1 μs delay between pulses, and a variable τ delay spanning a 0.001 - 50 s range.

The ^{39}K MAS NMR data from the $Cs_2K_xAg_{1-x}In_xCl_6$:Bi (x = 0 - 1) nanocrystal series were acquired at 20.0 T using Bruker Avance HD-850 (Larmor frequency ν_o = 39.67 MHz) spectrometer and a Bruker 4 mm HX probe operating at a MAS frequency of 12 kHz. Pulse time and chemical shift calibration were undertaken using solid KBr, where a non-selective ('solution') π/2 pulse time of 10 μs was measured corresponding to a selective ('solids') π/2 pulse time 5 μs for the I = 3/2 nucleus, and where the secondary solid KBr shift (δ_{iso} 55.1 ppm) is standardised against the 0.1 M KCl solution IUPAC primary reference (δ 0.0 ppm).[2] All ^{39}K MAS NMR data was acquired using a rotor-synchronised Hahn-echo (θ-τ-2θ-τ-acq.) experiment using a $\pi/2/\pi$ pulse pair of 5 and 10 μs, respectively, a recycle delay of 5 s, and a rotor-synchronised τ delay of 83.33 μs. The ^{39}K T_1 measurements were performed using the saturation-recovery pulse technique which utilised a saturation pulse train of 300 π/2 pulses of 5 μs duration, a 10 μs delay between pulses, and a variable τ delay spanning a 0.0011 - 10 s range.

DFT Calculations and Materials Modelling

Ab initio calculations were performed using the CASTEP density functional theory (DFT) package which employs planewave basis fucntions and ultrasoft pseudopotentials.[3] Each input

file was generated using the cif2cell package[4] and the Atomic Simulation Environment.[5] The regularised SCAN exchange-correlation functional[6] has been used throughout with consistent, on-the-fly ultrasoft pseudopotential generation.[7] SCAN has been shown to accurately describe the electronic and geometrical structure of perovskite materials.[8] Geometry optimisation were performed on all systems, with atomic position and lattice parameter relaxation being permitted; in these adjustments the 'FINE' basis precision setting in CASTEP and k-point grids that correspond to cubic supercells of approximately 20 Å lattice parameters were used. All NMR parameters were calculated using the GIPAW method using a 600 eV planewave cut-off for all compounds.[9, 10] The accuracy of the calculated chemical shieldings against the experimentally measured chemical shifts was established by comparison with NMR parameters from previously measured reference compounds. As demonstrated by the ^{133}Cs chemical shift calibration in Figure S8a an excellent linear relationship for the CsCl/$CsClO_4$/Cs_2SO_4 series was established;[11] however, for the perovskite materials studied in this work it was necessary to include and an additional shift to align the experimental and computed values. Hence, a small recalibration using the experimental and calculated NMR parameters from the $Cs_2AgInCl_6$ and $Cs_2AgBiCl_6$ systems was introduced (see Figure S8a) A similar ^{39}K chemical shift calibration was undertaken using the KF/KCl/KBr/KI/$KClO_4$/KIO_4 series as shown in Figure S8b.[12]

To model the effect of K^+ cation incorporation on the structural speciation and order, and the implications for the interpretation of the measured ^{133}Cs and ^{39}K MAS NMR data, a constrained variation of the *Ab Initio* Random Structure Search (AIRSS) method was introduced to generate ensembles of perturbed initial configurations by applying random rotations on the $[InCl_6]^{3-}$ and $[BiCl_6]^{3-}$ octahedra.[13] This was followed by subsequent geometry relaxation. This method has been successfully used to discover novel phases of materials.[14]

Band structure calculations were performed on the relaxed structures at a k-point density corresponding to cubic supercells of approximately 60 Å lattice parameters. It has been suggested that band gaps obtained from the SCAN functional using the generalised Kohn-Sham theory are more realistic than those calculated using Generalised Gradient Approximation (GGA) functionals with the multiplicative Kohn-Sham potential.[15] The calculations in this study only include scalar relativistic effects introduced via the pseudopotential construction. Although spin-orbit coupling interactions have been shown to affect the band structure if heavy atoms are present,[16] the qualitative interpretation is not impacted.[17] Density-of-states and the optical absorption spectrum calculations were performed using OptaDOS,[18] while the atomic structures were visualised using the AtomEye package.[19]

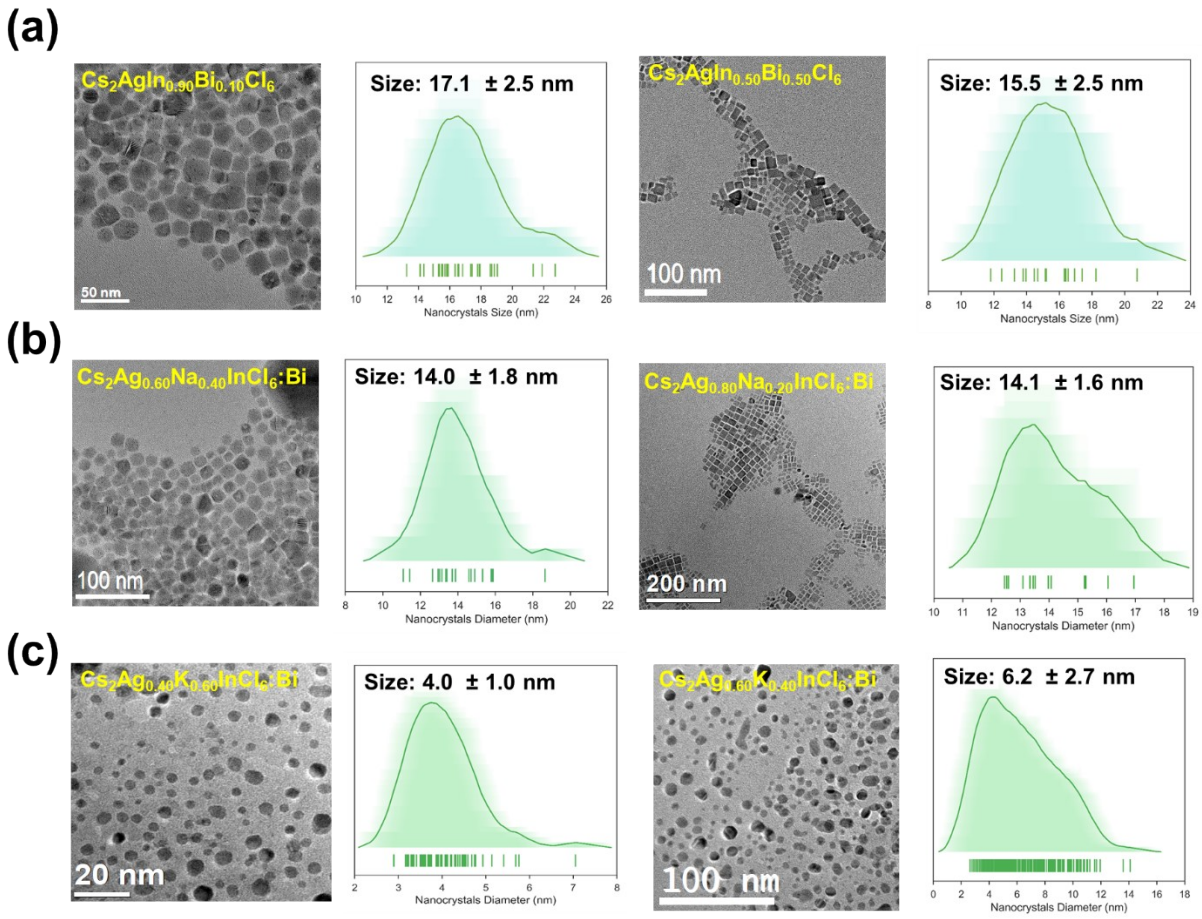

Figure S1. Additional TEM images and histogram analyses of (a) $Cs_2AgIn_{0.90}Bi_{0.10}Cl_6$ and $Cs_2AgIn_{0.50}Bi_{0.50}Cl_6$, (b) $Cs_2Ag_{0.60}Na_{0.40}InCl_6$:Bi and $Cs_2Ag_{0.80}Na_{0.20}InCl_6$:Bi, and (c) $Cs_2Ag_{0.40}K_{0.60}InCl_6$:Bi and $Cs_2Ag_{0.60}K_{0.40}InCl_6$:Bi nanocrystals.

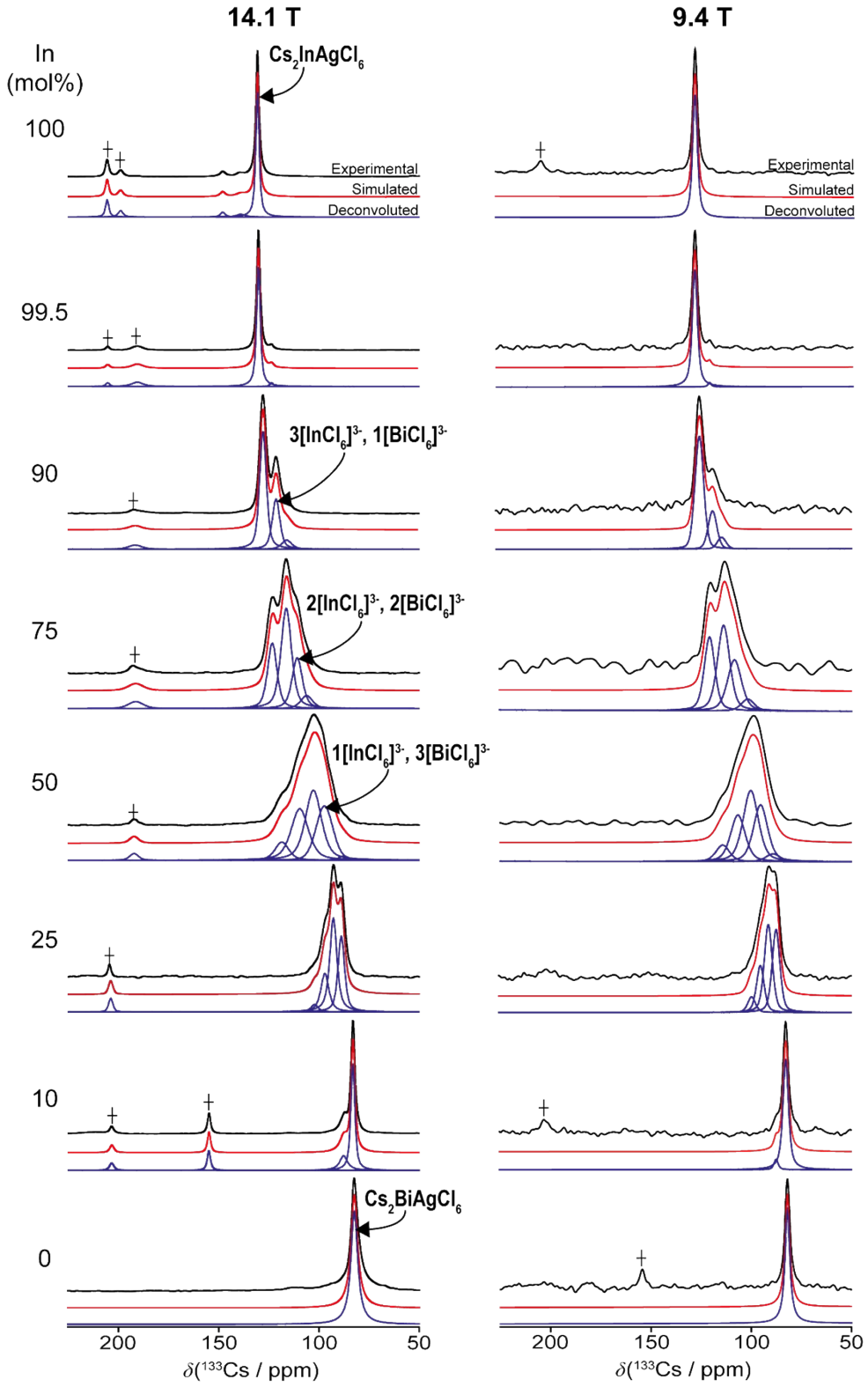

Figure S2. ^{133}Cs MAS NMR data (ν_r = 12 kHz) from the $Cs_2In_xBi_{1-x}AgCl_6$ (x = 0 - 1) nanocrystal series measured at magnetic field strengths of 14.1 and 9.4 T. Spectral simulations and deconvolutions are shown together with resonance assignments for the different octahedral substitution arrangements about each Cs position. The resonances attributed to impurities are indicated with a '†'.

Table S1. The ^{133}Cs isotropic chemical shifts (δ_{iso}), relative intensities, full-width-half-maximum (FWHM) and T_1 relaxation time data from the $Cs_2In_xBi_{1-x}AgCl_6$ (x = 0 - 1) nanocrystal compositional series measured at magnetic field strengths of 14.1 and 9.4 T (see Figure S2). The T_1 values were determined using the saturation-recovery technique.

In content (%)	Site	14.1 T				9.4 T			
		δ_{iso} (±1 ppm)	Rel. Int. (± 2 %)	FWHM (± 20 Hz)	T_1 (± 20 s)	δ_{iso} (±1 ppm)	Rel. Int. (± 2 %)	FWHM (± 20 Hz)	T_1 (± 20 s)
100	**$Cs_2InAgCl_6$**	128	100	160	290	128	100	150	200
99.5	**3[$InCl_6$]$^{3-}$, 1[$BiCl_6$]$^{3-}$**	121	3	170	420	121	2	110	350
	$Cs_2InAgCl_6$	128	97	170	720	127	98	160	500
90	**2[$InCl_6$]$^{3-}$, 2[$BiCl_6$]$^{3-}$**	114	7	360	360	114	7	260	320
	3[$InCl_6$]$^{3-}$, 1[$BiCl_6$]$^{3-}$	119	30	350	490	119	23	260	440
	$Cs_2InAgCl_6$	126	63	310	500	125	70	260	400
75	**1[$InCl_6$]$^{3-}$, 3[$BiCl_6$]$^{3-}$**	104	7	560	270	102	6	400	230
	2[$InCl_6$]$^{3-}$, 2[$BiCl_6$]$^{3-}$	109	22	480	400	108	26	430	260
	3[$InCl_6$]$^{3-}$, 1[$BiCl_6$]$^{3-}$	114	45	490	440	114	39	380	270
	$Cs_2InAgCl_6$	121	26	440	470	121	29	430	290
50	**$Cs_2BiAgCl_6$**	87	1	780	70	89	4	440	20
	1[$InCl_6$]$^{3-}$, 3[$BiCl_6$]$^{3-}$	96	26	780	270	95	28	440	80
	2[$InCl_6$]$^{3-}$, 2[$BiCl_6$]$^{3-}$	102	36	750	260	100	37	470	110
	3[$InCl_6$]$^{3-}$, 1[$BiCl_6$]$^{3-}$	109	29	800	100	107	23	450	60
	$Cs_2InAgCl_6$	118	8	740	30	114	8	420	30
25	**$Cs_2BiAgCl_6$**	88	32	300	340	88	34	240	200
	1[$InCl_6$]$^{3-}$, 3[$BiCl_6$]$^{3-}$	92	44	330	270	91	39	250	200
	2[$InCl_6$]$^{3-}$, 2[$BiCl_6$]$^{3-}$	96	20	330	340	95	20	240	210
	3[$InCl_6$]$^{3-}$, 1[$BiCl_6$]$^{3-}$	102	4	270	30	100	7	240	170
10	**$Cs_2BiAgCl_6$**	83	77	190	400	83	93	170	300
	1[$InCl_6$]$^{3-}$, 3[$BiCl_6$]$^{3-}$	87	23	170	280	88	7	130	220
0	**$Cs_2BiAgCl_6$**	82	100	170	220	82	100	150	200

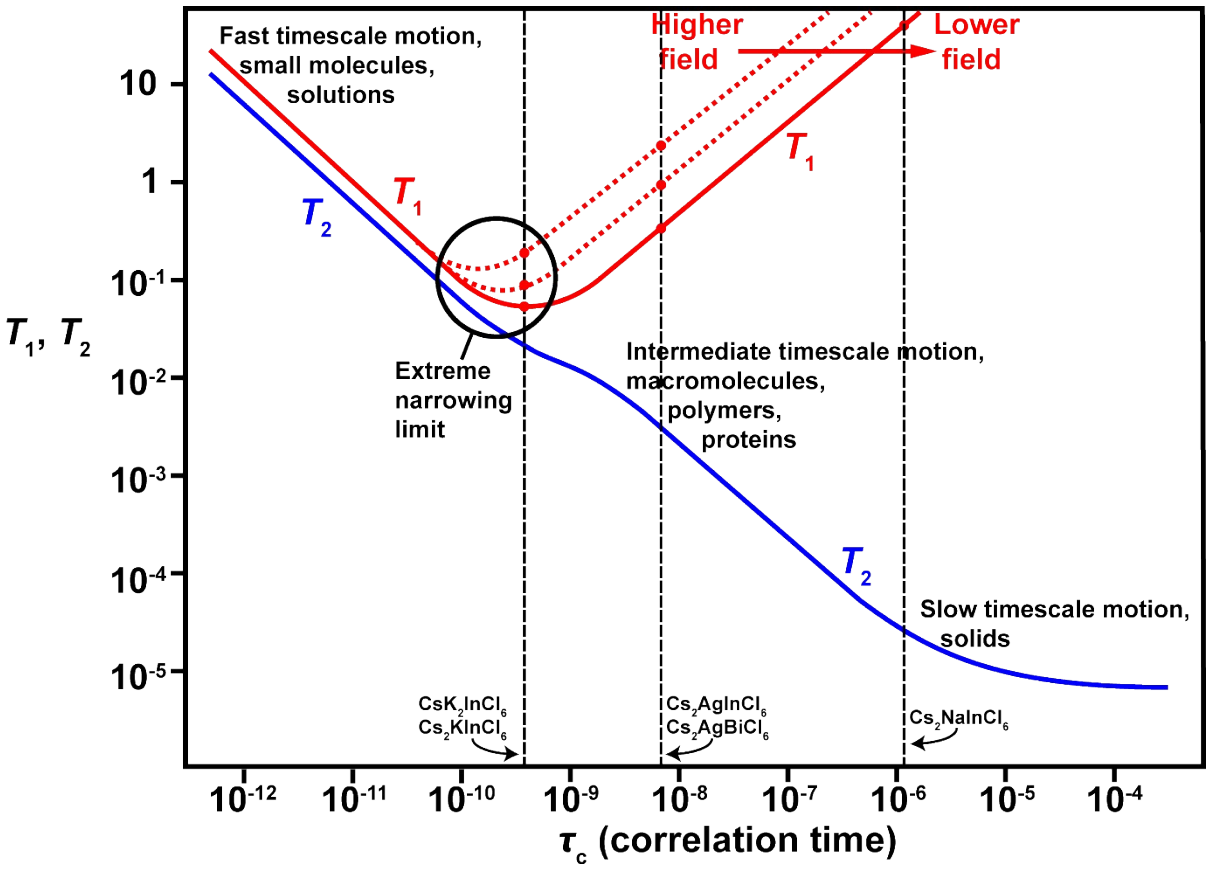

Figure S3. A diagrammatic representation showing the variation in longitudinal (T_1) and transverse (T_2) relaxation times with correlation time of motion (τ_c) under the influence of a dipolar relaxation mechanism. The approximate location of ^{133}Cs T_1 relaxation times from the Cs_2AInCl_6 (A = Na, K) and Cs_2AgBCl_6 (B = In, Bi) systems determined from saturation-recovery experiments are indicated, highlighting the large variations in reported T_1 values and Cs^+ mobility within these materials.

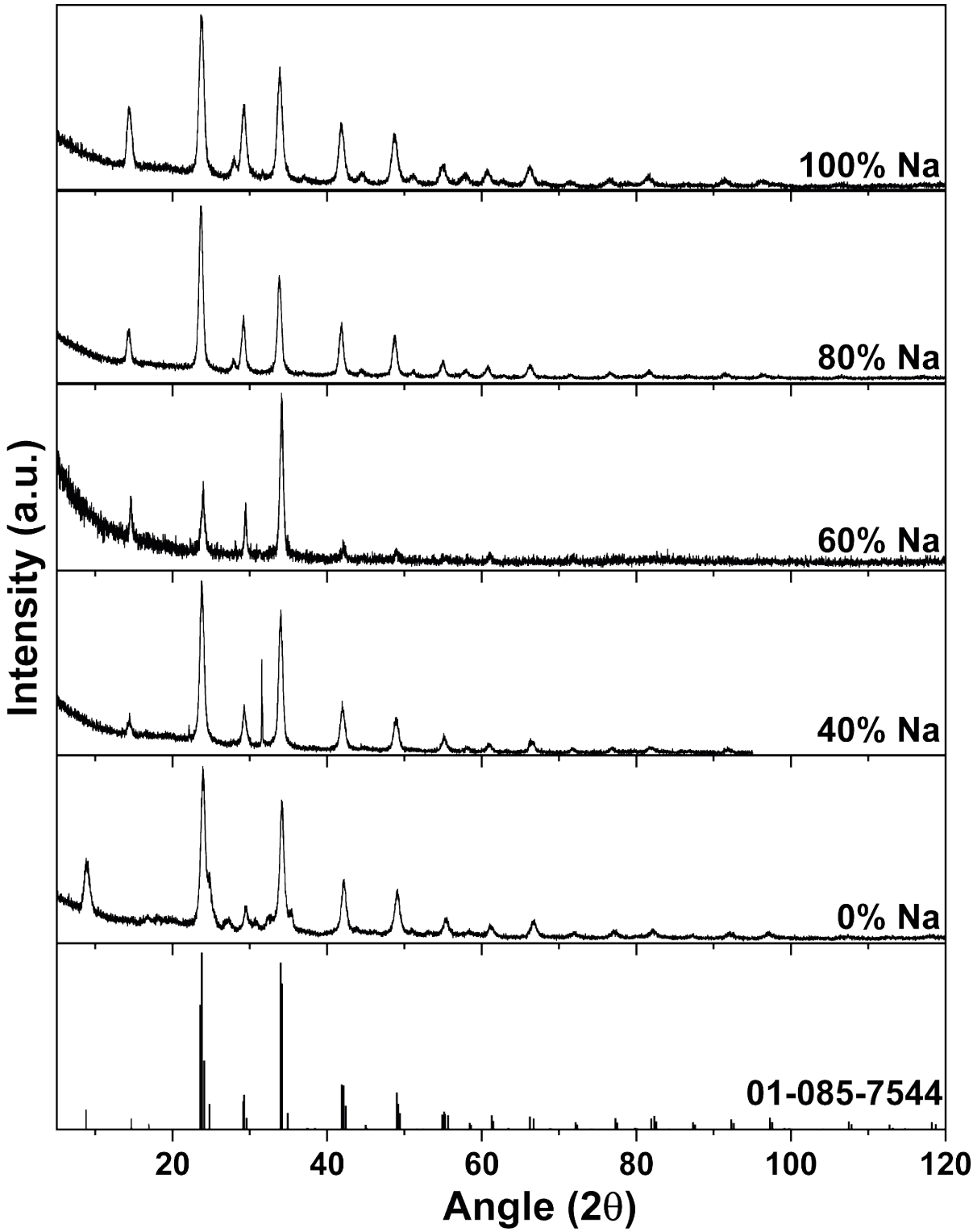

Figure S4. Powder X-ray diffraction data from the $Cs_2Na_xAg_{1-x}InCl_6$:Bi (x = 0 - 1) nanocrystal series. All diffraction peaks were matched against a standard $Cs_2AgInCl_6$ cubic perovskite phase (PDF: 01-085-7544).

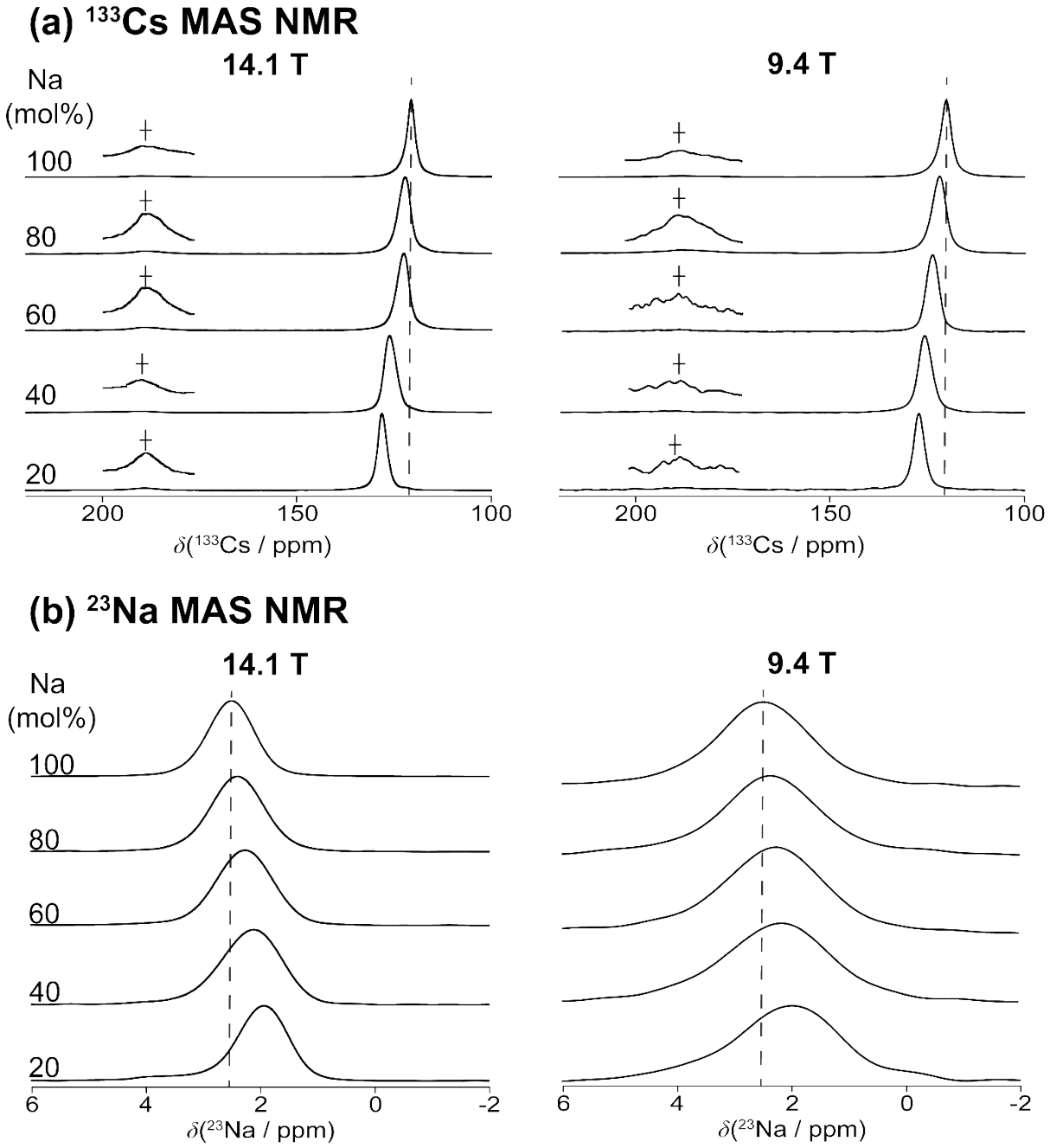

Figure S5. Solid state NMR study of the $Cs_2Na_xAg_{1-x}InCl_6$:Bi (x = 0.2 - 1) nanocrystal series showing (a) ^{133}Cs MAS NMR data (B_0 = 14.1 & 9.4 T, ν_r = 12 kHz), (b) ^{23}Na MAS NMR data (B_0 = 14.1 & 9.4 T, ν_r = 12 kHz). The low-intensity resonance in the ^{133}Cs MAS NMR data at δ ~190 ppm denoted with a '†' indicates the presence of a minor $CsInCl_4$ impurity.

Table S2. The (a) ^{133}Cs NMR parameters, and (b) ^{23}Na NMR parameters, including isotropic chemical shifts (δ_{iso}), full-width-half-maximum (FWHM) and T_1 relaxation time data from the $Cs_2Na_xAg_{1-x}InCl_6$:Bi (x = 0.2 - 1) nanocrystal series measured at magnetic field strengths of 14.1 and 9.4 T (see Figure S5). The T_1 values were determined using the saturation-recovery technique.

(a)

Na content (%)	Site	^{133}Cs					
		14.1 T			9.4 T		
		δ_{iso} (± 0.5 ppm)	FWHM (± 10 Hz)	T_1 (± 10 s)	δ_{iso} (± 0.5 ppm)	FWHM (± 10 Hz)	T_1 (± 10 s)
100	**$Cs_2InNaCl_6$/ $Cs_2InAgCl_6$**	120.9	200	450	120.2	190	380
80	**$Cs_2InNaCl_6$/ $Cs_2InAgCl_6$**	122.6	290	410	122.2	190	390
60	**$Cs_2InNaCl_6$/ $Cs_2InAgCl_6$**	124.5	300	780	123.8	200	470
40	**$Cs_2InNaCl_6$/ $Cs_2InAgCl_6$**	126.5	270	740	125.8	220	590
20	**$Cs_2InNaCl_6$/ $Cs_2InAgCl_6$**	128.0	230	720	127.3	180	450

(b)

Na content (%)	Site	^{23}Na					
		14.1 T			9.4 T		
		δ_{iso} (± 0.2 ppm)	FWHM (± 10 Hz)	T_1 (± 1 s)	δ_{iso} (± 0.2 ppm)	FWHM (± 10 Hz)	T_1 (± 1 s)
100	**$Cs_2InNaCl_6$**	2.5	180	10	2.5	220	9
80	**$Cs_2InNaCl_6$**	2.4	190	9	2.4	210	10
60	**$Cs_2InNaCl_6$**	2.3	210	11	2.3	230	10
40	**$Cs_2InNaCl_6$**	2.1	200	11	2.2	230	9
20	**$Cs_2InNaCl_6$**	2.0	180	11	2.0	230	10

Table S3. TEM EDXS data of $Cs_2AgIn_xBi_{1-x}Cl_6$, $Cs_2Na_xAg_{1-x}InCl_6$:Bi, and $Cs_2K_xAg_{1-x}InCl_6$:Bi nanocrystals. The average relative elemental ratios of inorganic constituent are in good agreement with the starting material proportions.

Sample	Cs	Na/K	Ag	In	Bi	Cl
$Cs_2AgInCl_6$	1.96	0	1.08	0.98	0	6.0
$Cs_2AgIn_{0.995}Bi_{0.05}Cl_6$	1.96	0	1.06	0.98	0.006	6.0
$Cs_2AgIn_{0.90}Bi_{0.10}Cl_6$	1.98	0	1.06	0.88	0.10	6.0
$Cs_2AgIn_{0.75}Bi_{0.25}Cl_6$	1.98	0	1.06	0.76	0.28	6.0
$Cs_2AgIn_{0.50}Bi_{0.50}Cl_6$	1.94	0	1.06	0.54	0.52	6.0
$Cs_2AgIn_{0.25}Bi_{0.75}Cl_6$	2.00	0	1.06	0.22	0.74	6.0
$Cs_2AgIn_{0.10}Bi_{0.90}Cl_6$	2.04	0	1.06	0.08	0.90	6.0
$Cs_2Na_{0.20}Ag_{0.80}InCl_6$:Bi	1.96	0.16	0.78	1.04	0.004	6.0
$Cs_2Na_{0.40}Ag_{0.60}InCl_6$:Bi	1.94	0.38	0.66	1.02	0.006	6.0
$Cs_2Na_{0.60}Ag_{0.40}InCl_6$:Bi	2.00	0.58	0.42	0.98	0.006	6.0
$Cs_2Na_{0.80}Ag_{0.20}InCl_6$:Bi	1.94	0.72	0.22	0.98	0.008	6.0
$Cs_2Na_{1.0}Ag_0InCl_6$:Bi	1.90	0.92	0	1.00	0.008	6.0
$Cs_2K_{0.20}Ag_{0.80}InCl_6$:Bi	1.90	0.18	0.82	1.02	0.010	6.0
$Cs_2K_{0.40}Ag_{0.60}InCl_6$:Bi	1.98	0.42	0.56	1.02	0.006	6.0
$Cs_2K_{0.60}Ag_{0.40}InCl_6$:Bi	1.92	0.62	0.42	1.02	0.004	6.0
$Cs_2K_{0.80}Ag_{0.40}InCl_6$:Bi	1.96	0.84	0.18	0.96	0.008	6.0
$Cs_2K_{1.0}Ag_0InCl_6$:Bi	1.90	1.08	0	0.98	0.004	6.0

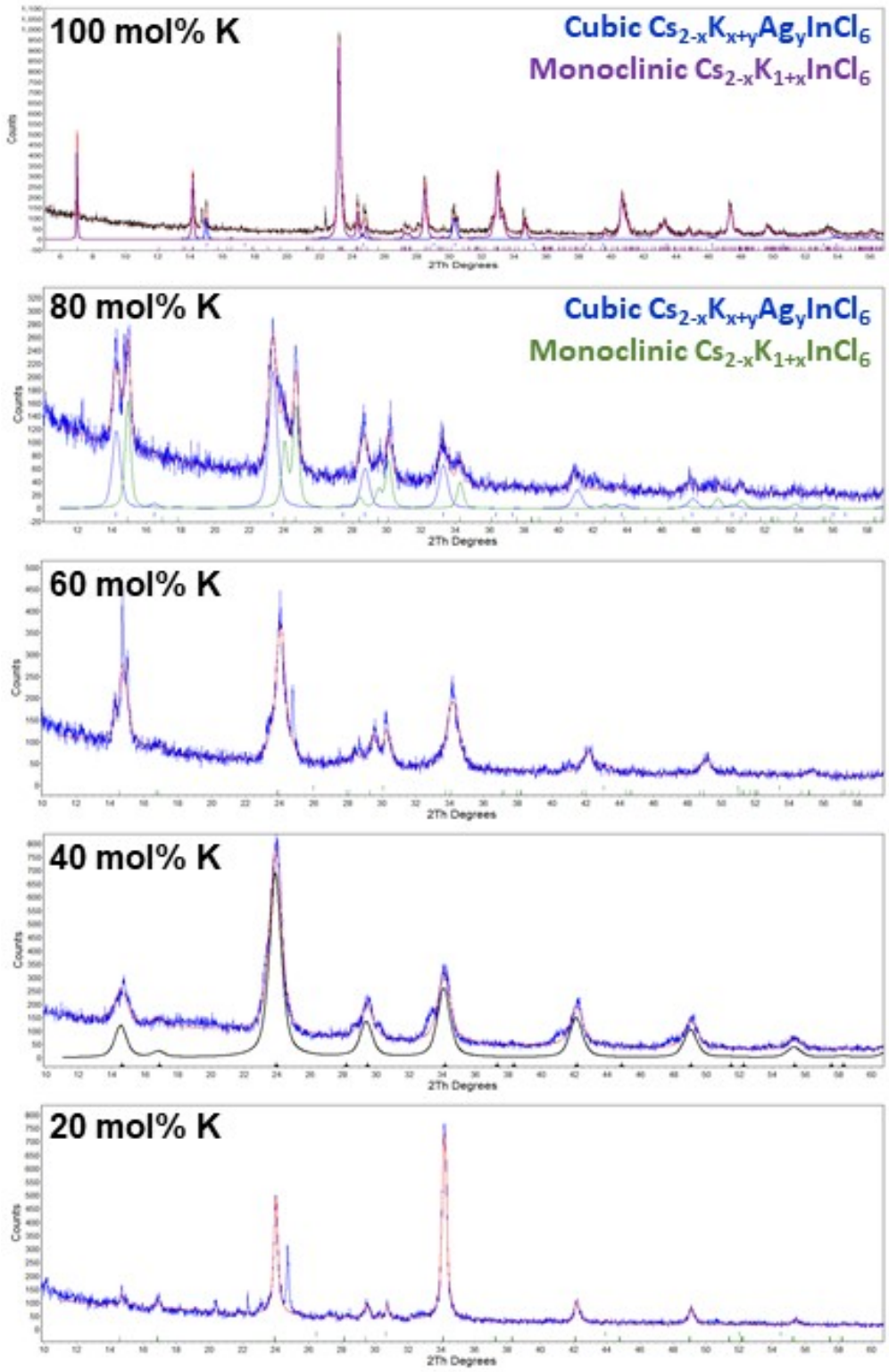

Figure S6. Powder XRD data from the $Cs_2K_xAg_{1-x}InCl_6$:Bi (x = 0.2 - 1) nanocrystals series. All the samples exhibit a component of the cubic double perovskite structure; however, a monoclinic K-bearing phase is also detected in the compositional range of x = 0.4 - 1. The lattice parameter variation with increasing mol % K^+ suggests substitution of this cation on the A and B'(I) positions in the double perovskite structure.

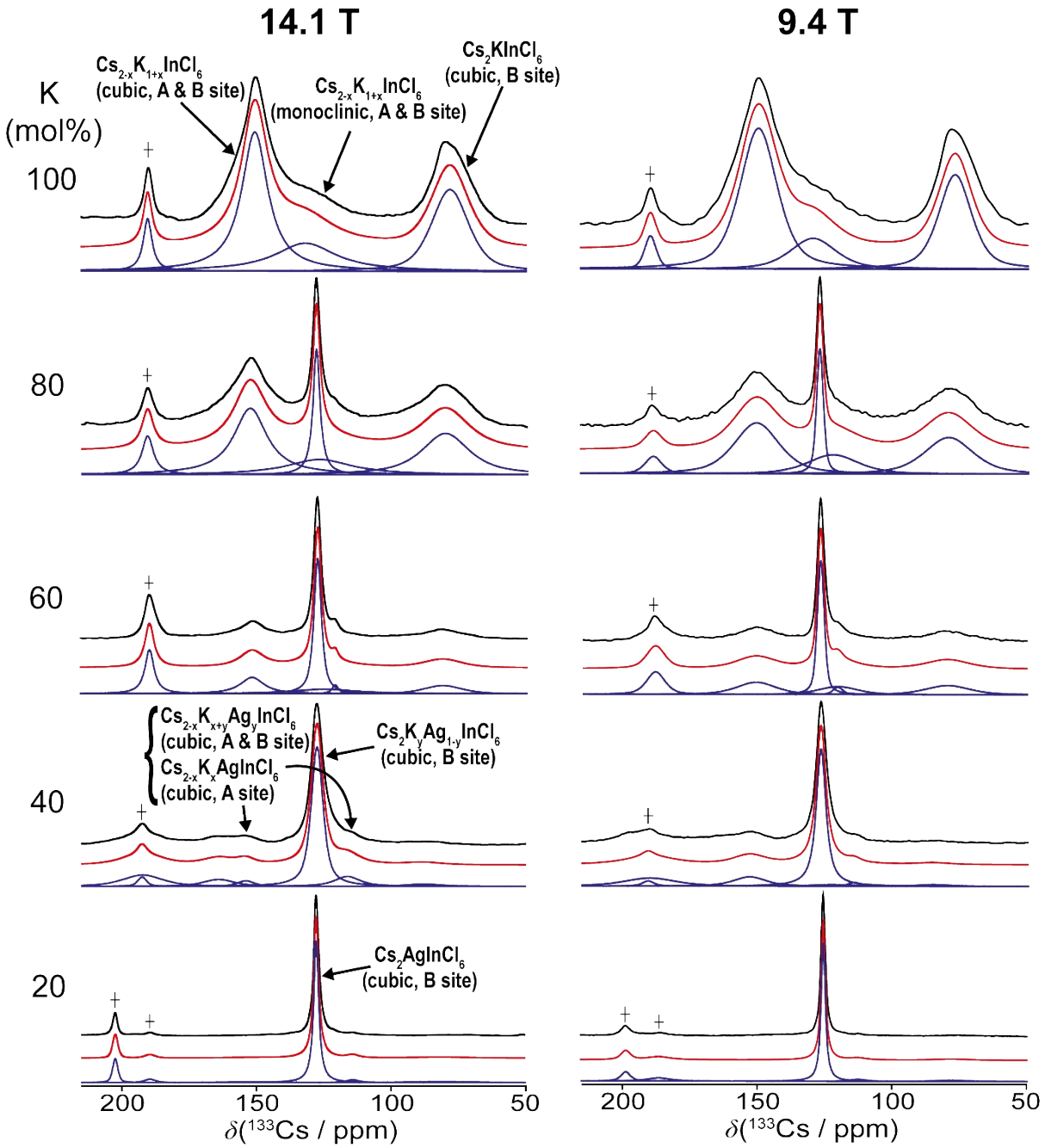

Figure S7. ^{133}Cs MAS NMR data (ν_r = 12 kHz) from the $Cs_2K_xAg_{1-x}InCl_6$:Bi (x = 0.2 - 1) nanocrystal series measured at magnetic field strengths of 14.1 and 9.4 T. Spectral simulations and deconvolutions are shown together with resonance assignments for the different octahedral substitution arrangements about each Cs position. The low-intensity resonance at δ ~190 ppm denoted with a '†' indicates the presence of a minor $CsInCl_4$ impurity.

Table S4. The ^{133}Cs isotropic chemical shifts (δ_{iso}), relative intensities, full-width-half-maximum (FWHM) and T_1 relaxation time data from the $Cs_2K_xAg_{1-x}InCl_6$:Bi (x = 0.2 - 1) nanocrystal series measured at magnetic field strengths of 14.1 and 9.4 T (see Figure S7). The T_1 values were determined using the saturation-recovery technique.

K content (%)	Site	14.1 T			9.4 T		
		δ (± 4 ppm)	T_1 (s)	FWHM (Hz, ±10%)	δ (± 4 ppm)	T_1 (s)	FWHM (Hz, ±10%)
100	Cs_2KInCl_6 (cubic, B site)	78	9 ± 3	1270	77	5 ± 3	800
	$Cs_{2-x}K_{1+x}InCl_6$ (monoclinic, A & B site)	132	6 ± 3	2160	129	5 ± 3	1180
	$Cs_{2-x}K_{1+x}InCl_6$ (cubic, A & B site)	151	3 ± 1	930	150	2 ± 1	880
80	Cs_2KInCl_6 (cubic, B site)	80	21 ± 3	1660	80	6 ± 3	1110
	$Cs_2AgInCl_6$ (cubic, B site) / $Cs_2K_yAg_{1-y}InCl_6$ (cubic, B site)	128	340 ± 20	240	127	220 ± 20	150
	$Cs_{2-x}K_{x+y}Ag_yInCl_6$ (cubic, A & B site) / $Cs_{2-x}K_xAgInCl_6$ (cubic, A site)	153	3 ± 1	1170	151	3 ± 1	1030
60	Cs_2KInCl_6 (cubic, B site)	82	18 ± 3	1420	80	8 ± 3	1010
	$Cs_2AgInCl_6$ (cubic, B site) / $Cs_2K_yAg_{1-y}InCl_6$ (cubic, B site)	128	490 ± 20	250	127	370 ± 20	160
	$Cs_{2-x}K_{x+y}Ag_yInCl_6$ (cubic, A & B site) / $Cs_{2-x}K_xAgInCl_6$ (cubic, A site)	152	6 ± 2	950	151	4 ± 2	900
40	$Cs_2AgInCl_6$ (cubic, B site) / $Cs_2K_yAg_{1-y}InCl_6$ (cubic, B site)	128	240 ± 20	410	127	160 ± 20	230
	$Cs_{2-x}K_{x+y}Ag_yInCl_6$ (cubic, A & B site) / $Cs_{2-x}K_xAgInCl_6$ (cubic, A site)	153	16 ± 3	590	154	12 ± 3	550
20	$Cs_2AgInCl_6$ bulk (cubic, B site)	128	500 ± 20	180	128	410 ± 20	100

Table S5. The ^{39}K isotropic chemical shifts (δ_{iso}), and T_1 relaxation time data from the $Cs_2K_xAg_{1-x}InCl_6$:Bi (x = 0.2 - 1) nanocrystal series measured at a magnetic field strength of 20.0 T (see Figure 7 in the main text). The T_1 values were determined using the saturation-recovery technique.

K content (%)	Site	20.0 T		
		δ (± 5 ppm)	T_1 (± 0.1 s)	Rel. Int. (± 3 %)
100	$Cs_{2-x}K_{1+x}InCl_6$ (cubic, A & B site) / $Cs_{2-x}K_{1+x}InCl_6$ (monoclinic, A & B site)	9	0.4	78
	$Cs_2K_yAg_{1-y}InCl_6$ (cubic, B site)	47	0.4	6
	Cs_2KInCl_6 (cubic, B site) / $Cs_{2-x}K_{1+x}InCl_6$ (cubic, A & B site) / $Cs_{2-x}K_{1+x}InCl_6$ (monoclinic, A & B site)	59	0.1	16
80	$Cs_{2-x}K_xAgInCl_6$ (cubic, A site) / $Cs_{2-x}K_{x+y}Ag_yInCl_6$ (cubic, A & B site)	14	-	73
	$Cs_2K_yAg_{1-y}InCl_6$ (cubic, B site)	47	-	11
	Cs_2KInCl_6 (cubic, B site) / $Cs_{2-x}K_{1+x}InCl_6$ (cubic, A & B site) / $Cs_{2-x}K_{1+x}InCl_6$ (monoclinic, A & B site)	59	-	16
60	$Cs_{2-x}K_xAgInCl_6$ (cubic, A site) / $Cs_{2-x}K_{x+y}Ag_yInCl_6$ (cubic, A & B site)	15	-	56
	$Cs_2K_yAg_{1-y}InCl_6$ (cubic, B site)	48	5.8	33
	Cs_2KInCl_6 (cubic, B site) / $Cs_{2-x}K_{1+x}InCl_6$ (cubic, A & B site) / $Cs_{2-x}K_{1+x}InCl_6$ (monoclinic, A & B site)	60	-	11
40	$Cs_{2-x}K_xAgInCl_6$ surface (cubic, A site) / $Cs_{2-x}K_{x+y}Ag_yInCl_6$ surface (cubic, A & B site)	15	-	91
	$Cs_2K_yAg_{1-y}InCl_6$ (cubic, B site)	48	-	9
20	$Cs_{2-x}K_xAgInCl_6$ surface (cubic, A site) / $Cs_{2-x}K_{x+y}Ag_yInCl_6$ surface (cubic, A & B site)	15	-	100

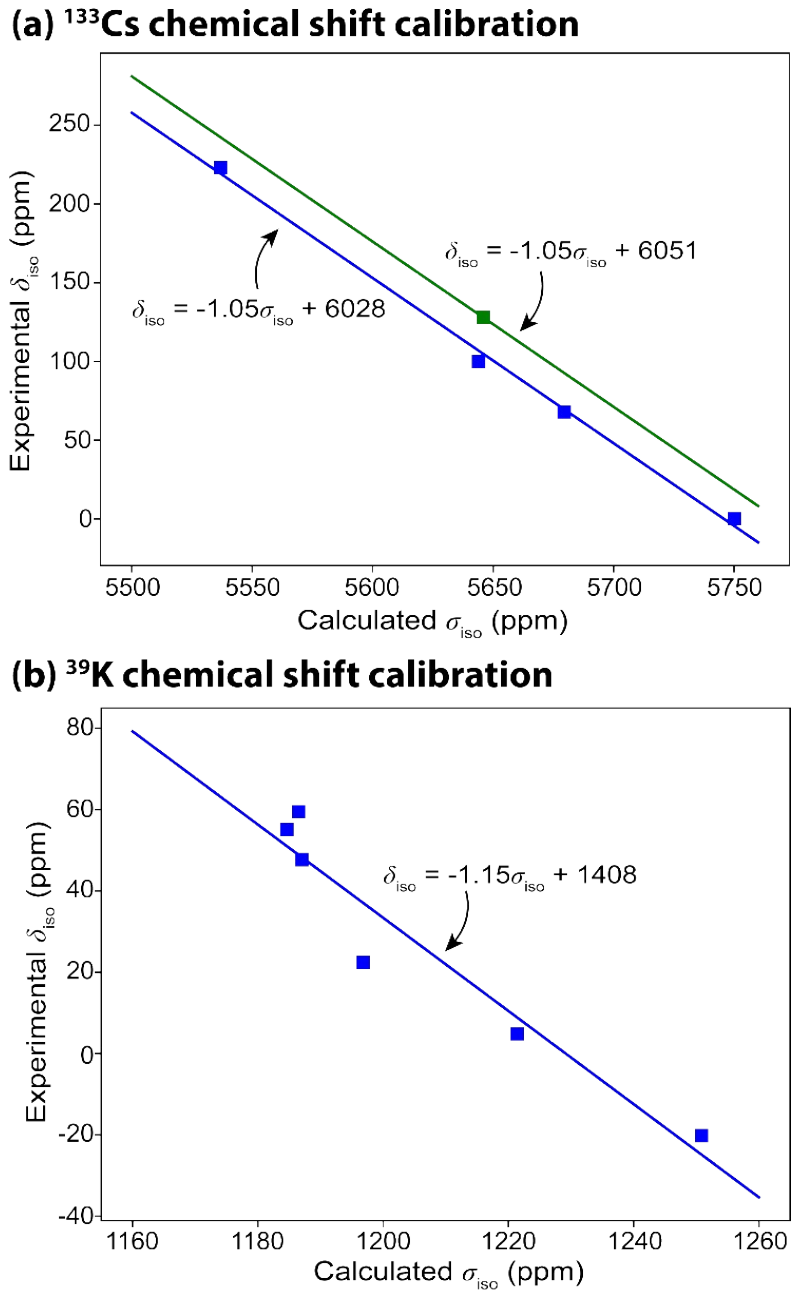

Figure S8. Calculated σ_{iso}/experimental δ_{iso} calibration curves relating, (a) the experimentally measured ^{133}Cs shifts and DFT calculated shieldings, and (b) the experimentally measured ^{39}K shifts and DFT calculated shieldings.

Table S6. Tauc plot estimation of the band gaps for all UV/vis absorption data presented in this work. It should be noted that these Tauc plot estimations calculate the band gap using a direct band gap of each material as the actual fundamental band gap is more complex as it is comprised of parity forbidden direct and indirect transitions.

Nanocrystal System	UV-vis Band Gap (eV)	Nanocrystal System	UV-vis Band Gap (eV)	Nanocrystal System	UV-vis Band Gap (eV)
0 mol% In^{3+}	3.38	20 mol% Na^{+}	3.42	20 mol% K^{+}	3.37
10 mol% In^{3+}	3.37	40 mol% Na^{+}	3.51	40 mol% K^{+}	3.39
25 mol% In^{3+}	3.35	60 mol% Na^{+}	3.60	60 mol% K^{+}	3.40
50 mol% In^{3+}	3.35	80 mol% Na^{+}	3.72	80 mol% K^{+}	3.59
75 mol% In^{3+}	3.34	100 mol% Na^{+}	3.83	100 mol% K^{+}	3.78
90 mol% In^{3+}	3.34				
99.5 mol% In^{3+}	3.36				

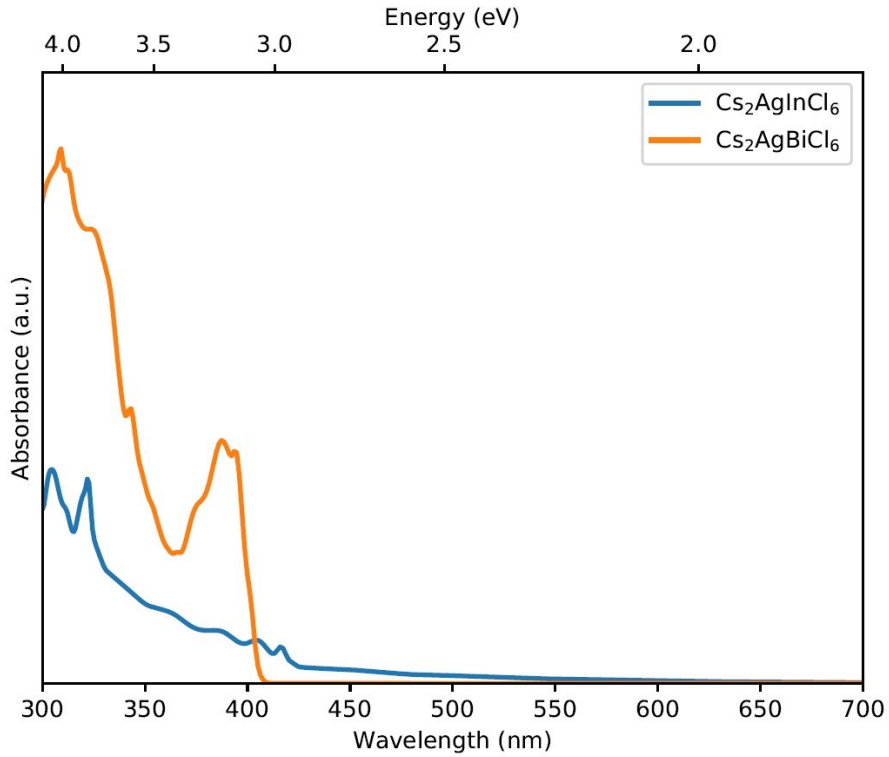

Figure S9. Calculated absorption spectra for the $Cs_2AgInCl_6$ and $Cs_2AgBiCl_6$ nanocrystal systems determined from band structure results. These semi-quantitatively corroborate the experimentally measured absorption data from these materials (see top and bottom spectra from Figure 1f).

References

1. D. Massiot, F. Fayon, M. Capron, I. King, S. Le Calvé, B. Alonso, J. O. Durand, B. Bujoli, Z. Gan and G. Hoatson, *Magnetic Resonance in Chemistry*, 2002, **40**, 70-76.
2. R. K. Harris, E. D. Becker, S. M. C. De Menezes, R. Goodfellow and P. Granger, *Pure and Applied Chemistry*, 2001, **73**, 1795-1818.
3. S. J. Clark, M. D. Segall, C. J. Pickard, P. J. Hasnip, M. I. Probert, K. Refson and M. C. Payne, *Zeitschrift für Kristallographie-Crystalline Materials*, 2005, **220**, 567-570.
4. T. Björkman, *Computer Physics Communications*, 2011, **182**, 1183-1186.
5. A. H. Larsen, J. J. Mortensen, J. Blomqvist, I. E. Castelli, R. Christensen, M. Dułak, J. Friis, M. N. Groves, B. Hammer and C. Hargus, *Journal of Physics: Condensed Matter*, 2017, **29**, 273002.
6. A. P. Bartók and J. R. Yates, *Journal of Chemical Physics*, 2019, **150**, 161101.
7. A. P. Bartók and J. R. Yates, *Physical Review B*, 2019, **99**, 235103.
8. M. Bokdam, J. Lahnsteiner, B. Ramberger, T. Schäfer and G. Kresse, *Physical Review Letters*, 2017, **119**, 145501.
9. C. J. Pickard and F. Mauri, *Physical Review B*, 2001, **63**, 245101.
10. J. R. Yates, C. J. Pickard and F. Mauri, *Physical Review B*, 2007, **76**, 024401.
11. S. Mooibroek, R. E. Wasylishen, R. Dickson, G. Facey and B. A. Pettitt, *Journal of Magnetic Resonance (1969)*, 1986, **66**, 542-545.
12. I. L. Moudrakovski and J. A. Ripmeester, *Journal of Physical Chemistry B*, 2007, **111**, 491-495.
13. C. J. Pickard and R. Needs, *Journal of Physics: Condensed Matter*, 2011, **23**, 053201.
14. C. J. Pickard and R. J. Needs, *Nature Physics*, 2007, **3**, 473-476.
15. J. P. Perdew, W. Yang, K. Burke, Z. Yang, E. K. Gross, M. Scheffler, G. E. Scuseria, T. M. Henderson, I. Y. Zhang and A. Ruzsinszky, *Proceedings of the National Academy of Sciences*, 2017, **114**, 2801-2806.
16. W. P. Huhn and V. Blum, *Physical Review Materials*, 2017, **1**, 033803.
17. W. Meng, X. Wang, Z. Xiao, J. Wang, D. B. Mitzi and Y. Yan, *Jjournal of Physical Chemistry Letters*, 2017, **8**, 2999-3007.
18. A. J. Morris, R. J. Nicholls, C. J. Pickard and J. R. Yates, *Computer Physics Communications*, 2014, **185**, 1477-1485.
19. J. Li, *Modelling and Simulation in Materials Science and Engineering*, 2003, **11**, 173.